Computational Mechanics 27 (2001) 445–462 © Springer-Verlag 2001

A specialized finite element for the study of woven composites

S. I. Haan, P. G. Charalambides, M. Suri

Abstract A specialized finite element is developed for the study of woven composites. The element utilizes an asymptotic displacement expansion comprised of the homogenized displacements and the local micro-displacements associated with the woven unit-cell elastostatics. Basic trigonometric functions first developed in [1], are employed as solutions to the local woven unit-cell problem under a general state of in-plane loading. The formulation also incorporates robust unit-cell geometry models for both polymer and ceramic matrix woven systems. As a result, the element can be used to predict not only the macroscopic homogeneous elastic response but also the microscopic elastic response of a finite geometry of a woven composite subjected to a general in-plane as well as transverse bending loading. The element performance is demonstrated by solving the finite geometry uniaxial tension problem and via near-tip studies for a crack under mode-I, mode-II, and mixed mode fracture conditions. In each case, the specialized element predictions are compared to known solutions for a corresponding cracked orthotropic material subjected to the same macroscopic loading conditions as well as the approximate solutions obtained using the well established 4-noded isoparametric plane elasticity element.

1 Introduction

Woven fabric composites are considered to be attractive material alternatives for many load bearing structures due to their superior fracture toughness, while retaining desirable mechanical properties such as stiffness, strength, oxidation, and creep resistance. A great deal [2–11] of research has been conducted for the purpose of analytically modeling the mechanical response of woven composites, while a few finite element models [11–14] have also been developed. The majority of these analytical models, however, are based on rather simple approximating assumptions regarding estimates of stresses and strains as well as the geometry of such systems, which may ultimately affect the reliability of these models. As a matter of fact, the development of accurate analytical models for woven composites has been rather challenging primarily due to the highly complex microstructure exhibited by such systems.

A typical unit-cell geometry of ceramic matrix woven composites developed in [15] is presented in Fig. 1a where the unit-cell is treated as a non-uniform 4-layered laminate. The micro-structure of the bundle is shown schematically in Fig. 1b. In order to properly model the unit-cell of ceramic matrix woven composites (see Fig. 1a) using the finite element method, (1) an effective homogenization scheme for the heterogeneous bundle phases (see Fig. 1b) is needed along with (2) a highly sophisticated meshing technique capable of accounting for the actual surface topology in the unit-cell.

In a recent study by Kuhn and Charalambides [16], where they modeled such systems using the finite element method, it was reported that approximately 800 20-noded isoparametric brick elements containing 15,000 degrees of freedom in total, were needed to obtain acceptable solutions for a complete unit-cell mesh (see Fig. 2). It was also reported that using the mesh stated above, it took about 40 min with the ABAQUS solver on an R-10000 (4-processor cluster) computer for a single linear solution. This rather conventional approach may be effective for a study of the linear response of a woven unit-cell. However, it seems to be highly computationally demanding for studying the non-linear response of a woven unit-cell, which may need hundreds of iterations for a converged solution. In light of the above, 3-D finite element modeling of woven finite geometry systems, if at all tractable, is expected to be computationally taxing and certainly inadequate in conducting non-linear studies that may require hundreds of iterations.

The 2-D isoparametric plane elasticity element with homogenized effective properties may be an effective alternative for a study on a finite geometry of woven composites under plane elasticity conditions. However, the

Received 27 November 2000

S. I. Haan, P. G. Charalambides (✉)
Department of Mechanical Engineering,
The University of Maryland Baltimore County,
1000 Hilltop Circle, Baltimore, MD 21250

M. Suri
Department of Mathematics and Statistics,
The University of Maryland Baltimore County,
1000 Hilltop Circle, Baltimore, MD 21250

S.I. Haan and P.G. Charalambides were partially supported by the National Science Foundation, Grant No. CMS94-96209 and by Technology Assessment and Transfer and Ceramic Composites Inc. of Anapolis, MD, USA. M. Suri was supported in part by the Air Force Office of Scientific Research, Air Force Systems Command, USAF under Grant F49620-98-0161 and by the National Science Foundation under Grant DMS 0074160. The authors would like to acknowledge useful discussions with J.L. Kuhn.

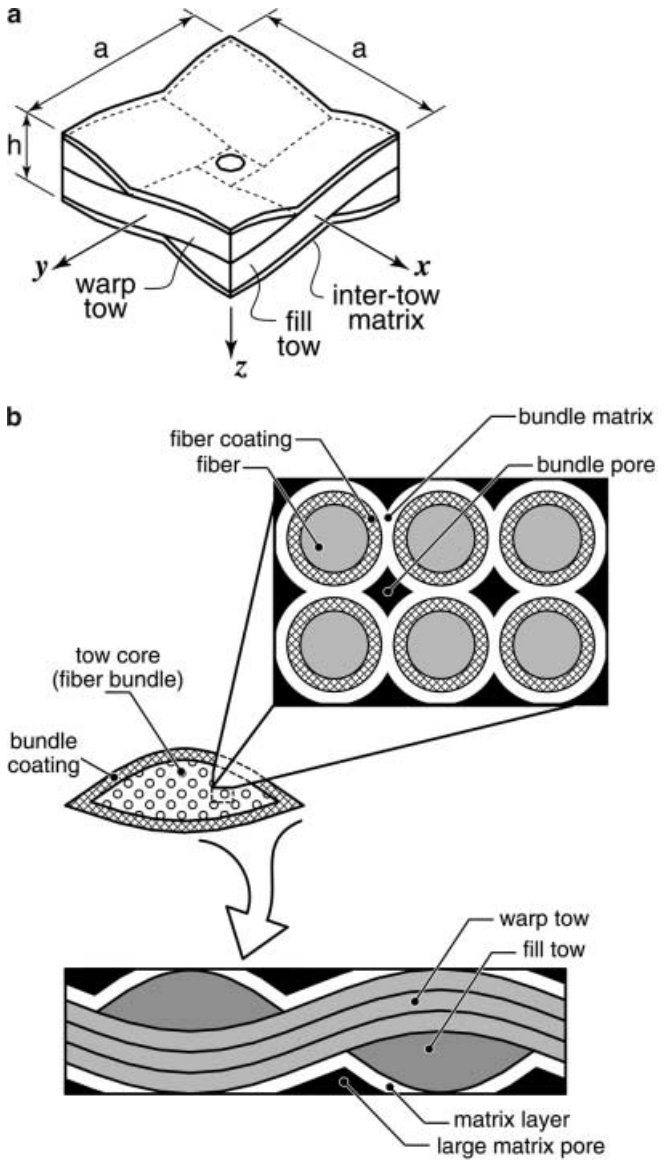

Fig. 1a, b. a The woven unit-cell comprised of warp tow, fill tow, and inter-tow matrix **b** Schematic of a typical Chemical Vapor Infiltrated (CVI) ceramic matrix plain weave fabric composite microstructure

results obtainable from this approach are limited to the homogenized mid-plane elastic fields, while the local micro-strains and micro-stresses, which are crucial in predicting the mechanical response, micro-damage evolution, and failure mechanism of such systems, cannot be obtained. Due to the difficulties stated above, most analytical approaches on such systems have been limited to modeling the mechanical response of a unit-cell and there has been an urgent need for the development of an effective and complete analysis tool to broaden the scope of such research.

In recent studies, Kuhn et al. [1] developed a semi-analytical approximate model capable of predicting accurate elastic micro-fields including displacements, micro-strains and micro-stresses of a woven unit-cell under a general in-plane loading condition. The solutions obtained from the model are compared favorably to those from 3-D finite element analysis, while retaining a superiority in computational efficiency. Furthermore, a series of non-linear microcracking damage models relying heavily on the semi-analytical approximate model [1] were also developed, to evaluate the state of micro-damage and capture the non-linear response of the woven unit-cell subjected to general in-plane loading conditions as addressed in [17–19]. These continuing efforts to analytically model both the linear and non-linear response of a woven unit-cell have established a firm foundation for the development of an effective analysis tool capable of predicting both the linear and non-linear response of finite geometry of woven composites. In addressing the above need, in this study, a specialized element for plain weave composites is proposed.

The element is developed on the basis of the semi-analytical approximate model by Kuhn et al. [1] and related micro-mechanics techniques including a unit-cell geometry model [15] and a hierarchical bundle homogenization scheme [20]. The symmetric part of the repeating unit-cell within which micro-fields such as displacements, micro-strains, and micro-stresses are accurately obtainable via the semi-analytical model [1], is designed to be a 4-noded finite element, superficially identical to the 4-noded isoparametric plane elasticity element. The displacement fields employed by the element exhibit an asymptotic expansion form comprised of the homogenized displacements and the local micro-displacements associated with the woven unit-cell. Specific unit-cell information such as the micro-structural geometry and related material properties is retained in the element formulation. The element carries all the information from the unit-cell while maintaining the simple characteristics of a conventional isoparametric plane elasticity element. As a result, the analysis using the element can provide not only the macroscopic mechanical response of the system but also the microscopic mechanical response, which up until now has been impossible to obtain through any other available techniques.

The structure of this paper is as follows. The formulation of the element is presented in Sect. 2. The 3-D displacement fields of the element are constructed using the concepts of the modified lamination theory first developed in [1] and interpolation techniques that yield the basic mid-plane micro-displacements in terms of the in-plane nodal displacements. Also in Sect. 2, micro-stresses and micro-strains in the interior of the element are derived in terms of the nodal displacements. In Sect. 3, the performance of the specialized element was studied with the aid of several finite geometry boundary value problems. An uni-axial tension specimen was used to establish deformed configuration, micro-stress fields for the corresponding boundary value problem. The element performance in regions of high stress gradients is further studied later in Sect. 3 by solving the asymptotic near-tip mode-I, mode-II, and mixed mode crack problems for which the 2-D analytical solutions for homogeneous orthotropic materials are known. Solution convergence and unit-cell size effects are also addressed for each of the above boundary value problems considered in Sect. 3. The approximate solution computed via the specialized element is compared to the exact solution for an orthotropic material with the same effective (homogenized) properties. The difference between the two is observed to decrease towards zero as

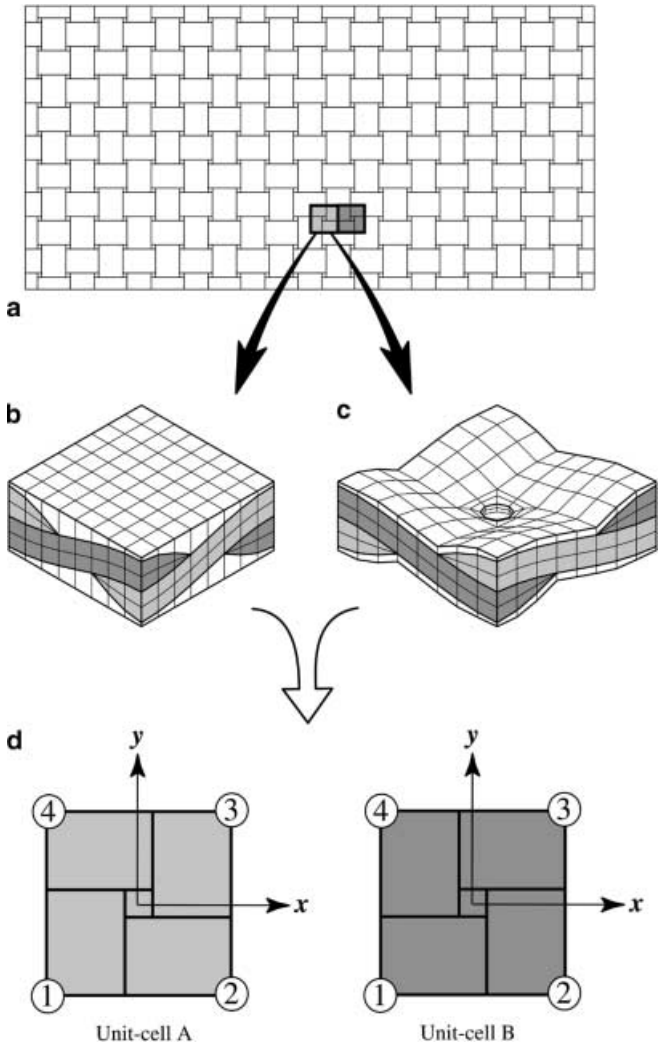

Fig. 2a–d. a The finite geometry of a typical woven composite. **b** The symmetric unit-cell of a PMC without large scale flaws. **c** The symmetric unit-cell of a CMC containing a large scale void. **d** The specialized element representing two different types of symmetric unit-cells

the cell-size a is reduced, indicating that the specialized element will pass the test of being asymptotically convergent as a approaches zero. Moreover, the order of this convergence is compared to that obtained with the 4-noded isoparametric plane elasticity element applied directly to the orthotropic material, and is observed to be identical in error measure. The near-tip micro-fields obtained for the mode-I crack problem are also presented. Concluding remarks are presented in Sect. 4.

2
Element formulation

The specialized finite element for woven composites proposed in this work is shown schematically in Fig. 2. The element represents the symmetric part of a repeating unit-cell, which is discussed in [15, 20]. More specifically, the symmetric part of the woven unit-cell is modeled through a 4-noded specialized finite element as shown in Fig. 2d with each node residing at the corresponding corner of the mid-plane of the unit-cell. As indicated in Fig. 2d, there exist two different types of symmetric unit-cells, which at a first glance appear to be associated with two different stiffness matrices. However, it has been found that the stiffness matrix of unit-cell A is identical to that of unit-cell B. Therefore, we used the stiffness matrix obtained from the unit-cell A (left-hand side of Fig. 2d) in constructing the finite element equations for the entire domain. On the other hand, during post-processing, we used both of the above unit-cell geometries as needed to appropriately calculate the geometry-dependent micro-strains and micro-stresses. The unit-cell of polymer matrix composites (PMCs) is presented in Fig. 2b and that of ceramic matrix composites (CMCs) is presented in Fig. 2c. As shown in Fig. 2c, the woven CMC unit-cell exhibits a large scale void that includes a depression of the matrix surfaces leading to an inter-connecting void at the center of the unit-cell. Thus, by employing the appropriate unit-cell, the proposed element is capable of accounting for both CMC and PMC systems. However, the emphasis shall be placed on CMCs rather than PMCs in this work. Extended discussion on the geometry of the woven unit-cell shown in Fig. 2 can be found in [15, 20].

2.1
Displacement interpolation

As mentioned above, each unit-cell is modeled by a two-dimensional specialized element which corresponds to its mid-plane (see Fig. 2d). Let the size of this element (the unit-cell size) be a. Then, associated with this element is a vector $\{u_N\} = \{u_1, v_1, u_2, v_2, u_3, v_3, u_4, v_4\}$ of unknown mid-plane displacements in the x- and y-direction for each node which will be the eventual unknowns in the finite element method. Under the fundamental assumptions made in the development of the semi-analytical technique for plain weave composites [1], the displacement components u, v, w at a point $p(x, y, z)$ in the interior of the unit-cell are given as follows:

$$\begin{Bmatrix} u(x,y,x) \\ v(x,y,z) \\ w(x,y) \end{Bmatrix} = \begin{Bmatrix} u_0 \\ v_0 \\ w_0 \end{Bmatrix} - z \begin{Bmatrix} w_{0,x} \\ w_{0,y} \\ 0 \end{Bmatrix} \tag{1}$$

The vector $\{u_0, v_0, w_0\}$ on the right-hand side of the above equation represents the spatially varying micro-displacements at the mid-plane of the woven unit-cell. Also in Eq. (1), $w_{0,x}$ and $w_{0,y}$ represent the partial derivatives of $w_0(x, y)$ with respect to x and y, respectively. In accordance with Eq. (1), the 3-D displacement fields in the reference woven unit-cell can be fully constructed within the context of the Kirchhoff-Love assumptions made in [1] by establishing the mid-plane micro-displacements $u_0(x, y)$, $v_0(x, y)$, and $w_0(x, y)$. In fact, Kuhn et al. in [1], established such fundamental solutions for certain canonical normalized in-plane loadings such as uniaxial tension in the x- and y-direction and in-plane pure shear. Appropriate trigonometric basis functions were used to express the solution (these are the test and trial functions in the Galerkin formulation of the problem). For instance, in the case of uniaxial tension in the x-direction, the solutions are expressed as follows:

$$\begin{Bmatrix} u_0 \\ v_0 \\ w_0 \end{Bmatrix}^x = \frac{1}{a}\left(\begin{bmatrix} x+\frac{a}{2} & 0 & 0 \\ -v_{xy}(y+\frac{a}{2}) & 0 & 0 \\ 0 & 0 & 0 \end{bmatrix} + a\begin{bmatrix} \bar{\Delta}_x^x & 0 & 0 \\ \bar{\Delta}_y^x & 0 & 0 \\ \bar{\Delta}_z^x & 0 & 0 \end{bmatrix}\right)\begin{Bmatrix} \hat{U}_x \\ 0 \\ 0 \end{Bmatrix} \quad (2)$$

In Eq. (2), the first matrix term on the right-hand side represents the homogeneous mid-plane displacements associated with the reciprocal unit-cell in-plane stretch $\hat{U}_x(=a\hat{\epsilon}_x^h)$ with $\hat{\epsilon}_x^h$ being homogeneous average strain. As discussed in [1], the in-plane Poisson's ratio v_{xy} appearing in Eq. (2) is also derived as a part of the solution. The second matrix term on the right-hand side of Eq. (2) represents the local (periodic) solutions of the given boundary value problem within the unit-cell. For example, $\bar{\Delta}_x^x$ represents the normalized mid-plane local (periodic) micro-displacement in the x-direction due to the applied uniform stretch $\hat{U}_x$. Using the same analogy, $\bar{\Delta}_y^x$ and $\bar{\Delta}_z^x$ represent mid-plane micro-displacement in the y- and z-direction due to $\hat{U}_x$, respectively. Again, consistent with [1], the above functions are:

$$\begin{aligned} \bar{\Delta}_x^x &= \sum_{m=1}^{M}\sum_{n=1}^{N} a_{mn}^x \sin\left[2m\pi\frac{x}{a}\right]\cos\left[2(n-1)\pi\frac{y}{a}\right] \\ \bar{\Delta}_y^x &= \sum_{m=1}^{M}\sum_{n=1}^{N} b_{mn}^x \cos\left[2(m-1)\pi\frac{x}{a}\right]\sin\left[2n\pi\frac{y}{a}\right] \\ \bar{\Delta}_z^x &= \sum_{m=1}^{M}\sum_{n=1}^{N} c_{mn}^x \sin\left[(2m-1)\pi\frac{x}{a}\right]\sin\left[(2n-1)\pi\frac{y}{a}\right] \end{aligned} \quad (3)$$

where superscript 'x' in the series coefficients (a_{mn}^x, b_{mn}^x, and c_{mn}^x) denote the boundary value problem (for this case, uniaxial tension in the x-direction) used in establishing the corresponding coefficients. Also in Eq. (3), M and N represent the number of coefficients used in the series solution as discussed in [1]. It is of importance to note that series solutions with more terms, yield more accurate micro-displacement fields of the corresponding boundary value problem as discussed in [1]. Throughout this study, M and N were set to be equal to 10, consistent with the convergence study presented in [1].

The structure and notation of solutions of other basic boundary value problems such as uniaxial tension in the y-direction and in-plane shear cases are analogous to those of the uniaxial tension in the x-direction case. The solutions of the uniaxial tension in the y-direction problem are given as follows:

$$\begin{Bmatrix} u_0 \\ v_0 \\ w_0 \end{Bmatrix}^y = \frac{1}{a}\left(\begin{bmatrix} 0 & -v_{yx}(x+\frac{a}{2}) & 0 \\ 0 & y+\frac{a}{2} & 0 \\ 0 & 0 & 0 \end{bmatrix} + a\begin{bmatrix} 0 & \bar{\Delta}_x^y & 0 \\ 0 & \bar{\Delta}_y^y & 0 \\ 0 & \bar{\Delta}_z^y & 0 \end{bmatrix}\right)\begin{Bmatrix} 0 \\ \hat{U}_y \\ 0 \end{Bmatrix} \quad (4)$$

with

$$\begin{aligned} \bar{\Delta}_x^y &= \sum_{m=1}^{M}\sum_{n=1}^{N} a_{mn}^y \sin\left[2m\pi\frac{x}{a}\right]\cos\left[2(n-1)\pi\frac{y}{a}\right] \\ \bar{\Delta}_y^y &= \sum_{m=1}^{M}\sum_{n=1}^{N} b_{mn}^y \cos\left[2(m-1)\pi\frac{x}{a}\right]\sin\left[2n\pi\frac{y}{a}\right] \\ \bar{\Delta}_z^y &= \sum_{m=1}^{M}\sum_{n=1}^{N} c_{mn}^y \sin\left[(2m-1)\pi\frac{x}{a}\right]\sin\left[(2n-1)\pi\frac{y}{a}\right] \end{aligned} \quad (5)$$

Also in [1], Kuhn et al. showed that the mid-plane micro-displacement fields for the pure shear problem are given as follows:

$$\begin{Bmatrix} u_0 \\ v_0 \\ w_0 \end{Bmatrix}^{\mathrm{sh}} = \frac{1}{a}\left(\begin{bmatrix} 0 & 0 & y+\frac{a}{2} \\ 0 & 0 & 0 \\ 0 & 0 & 0 \end{bmatrix} + a\begin{bmatrix} 0 & 0 & \bar{\Delta}_x^{\mathrm{sh}} \\ 0 & 0 & \bar{\Delta}_y^{\mathrm{sh}} \\ 0 & 0 & \bar{\Delta}_z^{\mathrm{sh}} \end{bmatrix}\right)\begin{Bmatrix} 0 \\ 0 \\ \hat{U}_{xy} \end{Bmatrix} \quad (6)$$

where

$$\begin{aligned} \bar{\Delta}_x^{\mathrm{sh}} &= \sum_{m=1}^{M}\sum_{n=1}^{N} a_{mn}^{\mathrm{sh}} \sin\left[(2m-1)\pi\frac{x}{a}\right]\cos\left[2n\pi\frac{y}{a}\right] \\ \bar{\Delta}_y^{\mathrm{sh}} &= \sum_{m=1}^{M}\sum_{n=1}^{N} b_{mn}^{\mathrm{sh}} \cos\left[2m\pi\frac{x}{a}\right]\sin\left[2(n-1)\pi\frac{y}{a}\right] \\ \bar{\Delta}_z^{\mathrm{sh}} &= \sum_{m=1}^{M}\sum_{n=1}^{N} c_{mn}^{\mathrm{sh}} \cos\left[(2m-1)\pi\frac{x}{a}\right]\cos\left[(2n-1)\pi\frac{y}{a}\right] \end{aligned} \quad (7)$$

Schematics depicting these three basic boundary value problems are shown in Fig. 3. Consistent with Fig. 3, the solutions given in Eqs. (2), (4), and (6) represent the mid-plane micro-displacements induced by the in-plane uniform stretches $\hat{U}_x$, $\hat{U}_y$, and shear $\hat{U}_{xy}$, respectively. A closer inspection of Eqs. (2), (4), and (6) reveals that each mid-plane displacement field obtained for the corresponding boundary value problem is of the following asymptotic expansion form:

$$\{u_0\}^k = ([\bar{u}^h]^k + a[\bar{\Delta}(\xi_1,\xi_2)]^k)\frac{1}{a}\{\hat{U}\} + \cdots \quad (8)$$

where $[\bar{u}^h]^k$ is the mean zero-order displacement matrix for the homogeneous medium, corresponding to the boundary value problem k $(=x,y,\mathrm{sh})$ and $\frac{1}{a}\{\hat{U}\}$ is the homogeneous average strain vector. Also in Eq. (8), $\xi_1 = x/a$, and $\xi_2 = y/a$. In [1], the normalized functions $[\bar{\Delta}]^k$ were expressed using approximate trigonometric basis functions, whose series coefficients were obtained by solving the local equations of elasto-statics within the unit-cell under the Kirchhoff-Love plate theory assumption. Also, the parametric studies performed for various geometric variables (see [16]) showed that the thin plate theory employed in this study would hold for a wide range of microstructural variations of the woven unit-cell aspect ratio $h/a \simeq 1.0$. In woven systems of higher h/a, the

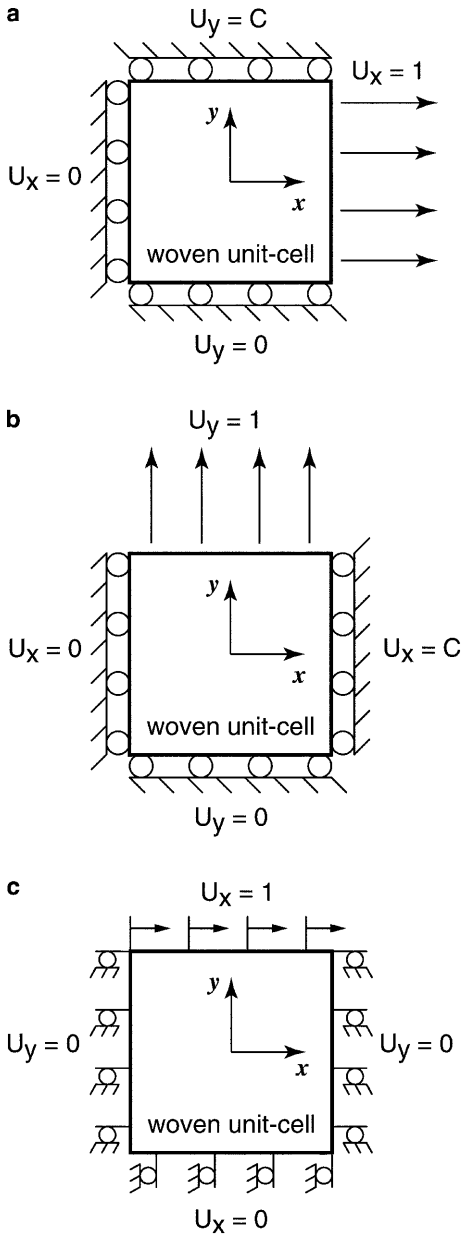

Fig. 3a–c. The boundary conditions imposed on the woven unit-cell. **a** uniaxial tension in the x-direction, **b** uniaxial tension in the y-direction, and **c** pure shear loading

assumption of cross-sectional planarity during deformation may be inadequate, which may appropriately limit the application of the element developed herein.

Therefore, the mid-plane micro-displacement fields in the interior of the element (woven unit-cell) subjected to a general in-plane loading can be obtained by linearly superimposing those three basic mid-plane micro-displacement fields given in Eqs. (2), (4), and (6) as follows:

$$\begin{Bmatrix} u_0 \\ v_0 \\ w_0 \end{Bmatrix} = \begin{Bmatrix} u_0 \\ v_0 \\ w_0 \end{Bmatrix}^{x} + \begin{Bmatrix} u_0 \\ v_0 \\ w_0 \end{Bmatrix}^{y} + \begin{Bmatrix} u_0 \\ v_0 \\ w_0 \end{Bmatrix}^{\mathrm{sh}} \tag{9}$$

Further expanding Eq. (9) with the aid of Eqs. (2), (4), and (6) and recognizing $\frac{1}{a}\{\hat{U}\} \equiv \{\hat{\epsilon}^h\}$, we get

$$\begin{aligned} \begin{Bmatrix} u_0 \\ v_0 \\ w_0 \end{Bmatrix} &= \left(\begin{bmatrix} x+\frac{a}{2} & -v_{yx}\left(x+\frac{a}{2}\right) & y+\frac{a}{2} \\ -v_{xy}\left(y+\frac{a}{2}\right) & y+\frac{a}{2} & 0 \\ 0 & 0 & 0 \end{bmatrix} \right. \\ &\quad \left. + a \begin{bmatrix} \bar{\Delta}_x^x & \bar{\Delta}_x^y & \bar{\Delta}_x^{\mathrm{sh}} \\ \bar{\Delta}_y^x & \bar{\Delta}_y^y & \bar{\Delta}_y^{\mathrm{sh}} \\ \bar{\Delta}_z^x & \bar{\Delta}_z^y & \bar{\Delta}_z^{\mathrm{sh}} \end{bmatrix} \right) \frac{1}{a} \begin{Bmatrix} \hat{U}_x \\ \hat{U}_y \\ \hat{U}_{xy} \end{Bmatrix} \\ &= \begin{bmatrix} \bar{N}_x^x & \bar{N}_x^y & \bar{N}_x^{\mathrm{sh}} \\ \bar{N}_y^x & \bar{N}_y^y & \bar{N}_y^{\mathrm{sh}} \\ \bar{N}_z^x & \bar{N}_z^y & \bar{N}_z^{\mathrm{sh}} \end{bmatrix} \begin{Bmatrix} \hat{\epsilon}_x^h \\ \hat{\epsilon}_y^h \\ \hat{\gamma}_{xy}^h \end{Bmatrix} \\ &= [\hat{N}]\{\hat{\epsilon}^h\} \ . \end{aligned} \tag{10}$$

In Eq. (10), the interpolation function $\hat{N}_i^j$ contains both the homogeneous part and the periodic (local) part $\bar{\Delta}_i^j$ of the mid-plane micro-displacements. Also, these functions implicitly account for the microstructure induced coupling between in-plane tension and shear as reported in [21] and reflected on the case study results discussed later on this study. Considering the effects of Poisson's ratio of the two uniaxial cases, we know that the normal components of the resulting homogeneous strains $\bar{\epsilon}_x^h$ and $\bar{\epsilon}_y^h$ are obtained as

$$\begin{cases} \bar{\epsilon}_x^h = \hat{\epsilon}_x^h - \delta\hat{\epsilon}_x^y = \hat{\epsilon}_x^h - v_{yx}\hat{\epsilon}_y^h \\ \bar{\epsilon}_y^h = \hat{\epsilon}_y^h - \delta\hat{\epsilon}_y^x = \hat{\epsilon}_y^h - v_{xy}\hat{\epsilon}_x^h \end{cases} \tag{11}$$

where $\delta\hat{\epsilon}_y^x$ and $\delta\hat{\epsilon}_x^y$ represent the additional strains induced due to the Poisson's ratio effects of the applied uniaxial stretches in the x- and y-direction ($\hat{U}_x$ and $\hat{U}_y$), respectively. Thus, the resulting homogeneous strain vector $\{\bar{\epsilon}^h\}$ can be expressed in terms of the applied homogeneous strain vector $\{\hat{\epsilon}^h\}$ in conjunction with the correction matrix $[D]$ as follows:

$$\begin{Bmatrix} \bar{\epsilon}_x^h \\ \bar{\epsilon}_y^h \\ \bar{\gamma}_{xy}^h \end{Bmatrix} = \begin{bmatrix} 1 & -v_{yx} & 0 \\ -v_{xy} & 1 & 0 \\ 0 & 0 & 1 \end{bmatrix} \begin{Bmatrix} \hat{\epsilon}_x^h \\ \hat{\epsilon}_y^h \\ \hat{\gamma}_{xy}^h \end{Bmatrix} = [D] \begin{Bmatrix} \hat{\epsilon}_x^h \\ \hat{\epsilon}_y^h \\ \hat{\gamma}_{xy}^h \end{Bmatrix} \tag{12}$$

In light of Eqs. (10) and (12), the mid-plane micro-displacement fields in the interior of the element is given in terms of the in-plane homogeneous strain vector $\{\bar{\epsilon}^h\}$ as follows:

$$\begin{Bmatrix} u_0 \\ v_0 \\ w_0 \end{Bmatrix} = [\bar{N}][D]^{-1} \begin{Bmatrix} \bar{\epsilon}_x^h \\ \bar{\epsilon}_y^h \\ \bar{\gamma}_{xy}^h \end{Bmatrix} \tag{13}$$

Now, it remains to express the in-plane homogeneous strains $\bar{\epsilon}_x^h$, $\bar{\epsilon}_y^h$, $\bar{\gamma}_{xy}^h$ in terms of the element nodal displacement vector $\{u_N\}$. Such a relationship can easily be established using the strain interpolations for the 4-noded plane elasticity element, which yields:

$$\begin{Bmatrix} \bar{\epsilon}_x^h \\ \bar{\epsilon}_y^h \\ \bar{\gamma}_{xy}^h \end{Bmatrix} = [A_0]\{u_N\} \ . \tag{14}$$

For this, we set

$$[A_0] = \begin{bmatrix} h_{1,x} & 0 & h_{2,x} & 0 & h_{3,x} & 0 & h_{4,x} & 0 \\ 0 & h_{1,y} & 0 & h_{2,y} & 0 & h_{3,y} & 0 & h_{4,y} \\ h_{1,y} & h_{1,x} & h_{2,y} & h_{2,x} & h_{3,y} & h_{3,x} & h_{4,y} & h_{4,x} \end{bmatrix} \tag{15}$$

where $h_{i,x}$ and $h_{i,y}$ represent the partial derivative of the shape function h_i with respect to x and y, respectively. The shape functions h_i used in Eq. (15) are:

$$\begin{aligned} h_1 &= \left(\frac{a}{2} - x\right)\left(\frac{a}{2} - y\right)\Big/ a^2 \\ h_2 &= \left(\frac{a}{2} + x\right)\left(\frac{a}{2} - y\right)\Big/ a^2 \\ h_3 &= \left(\frac{a}{2} + x\right)\left(\frac{a}{2} + y\right)\Big/ a^2 \\ h_4 &= \left(\frac{a}{2} - x\right)\left(\frac{a}{2} + y\right)\Big/ a^2 \end{aligned} \tag{16}$$

Hence, the mid-plane displacements can be expressed in terms of the nodal displacements $\{u_N\}$ as follows:

$$\begin{Bmatrix} u_0 \\ v_0 \\ w_0 \end{Bmatrix} = [\bar{N}][D]^{-1}[A_0]\{u_N\} = [R]\{u_N\} \tag{17}$$

where $[R] = [\bar{N}][D]^{-1}[A_0]$.

Next, we derive an expression for the 3-D micro-displacement fields in the interior of the element. Consistent with the theory and assumptions presented in [1], the out-of-plane displacement of the system $w(x, y)$ depends only on the coordinates x and y ($u_0(x, y)$ and $v_0(x, y)$), and as such can be captured in terms of the mid-plane displacement in the z-direction $w_0(x, y)$. According to the modified lamination theory (see Fig. 4) by which any differential column extracted from the unit-cell is treated as non-uniform 4-layered laminate (see [1] for the details), the displacement fields in the interior of the element are given as in Eq. (1). After further expanding Eq. (1) with the aid of Eq. (17), the final expression for the displacement fields $\{u\}$ are obtained in matrix form as follows:

$$\begin{aligned} \{u\} &= ([\bar{N}][D]^{-1}[A_0] - z([\bar{N}_w][D]^{-1}[A_0] \\ &\quad + [\bar{N}_x][D]^{-1}[A_0]_{,x} + [\bar{N}_y][D]^{-1}[A_0]_{,y}))\{u_N\} \\ &= [A]\{u_N\} \end{aligned} \tag{18}$$

The notations $[A_0]_{,x}$ and $[A_0]_{,y}$ in Eq. (18) represent the partial derivative of the matrix $[A_0]$ with respect to x and y, respectively. The auxiliary matrices appearing in Eq. (18) are as follows:

$$[\bar{N}_w] = \begin{bmatrix} \bar{N}^x_{z,x} & \bar{N}^y_{z,x} & \bar{N}^{sh}_{z,x} \\ \bar{N}^y_{z,y} & \bar{N}^y_{z,y} & \bar{N}^{sh}_{z,y} \\ 0 & 0 & 0 \end{bmatrix} \tag{19}$$

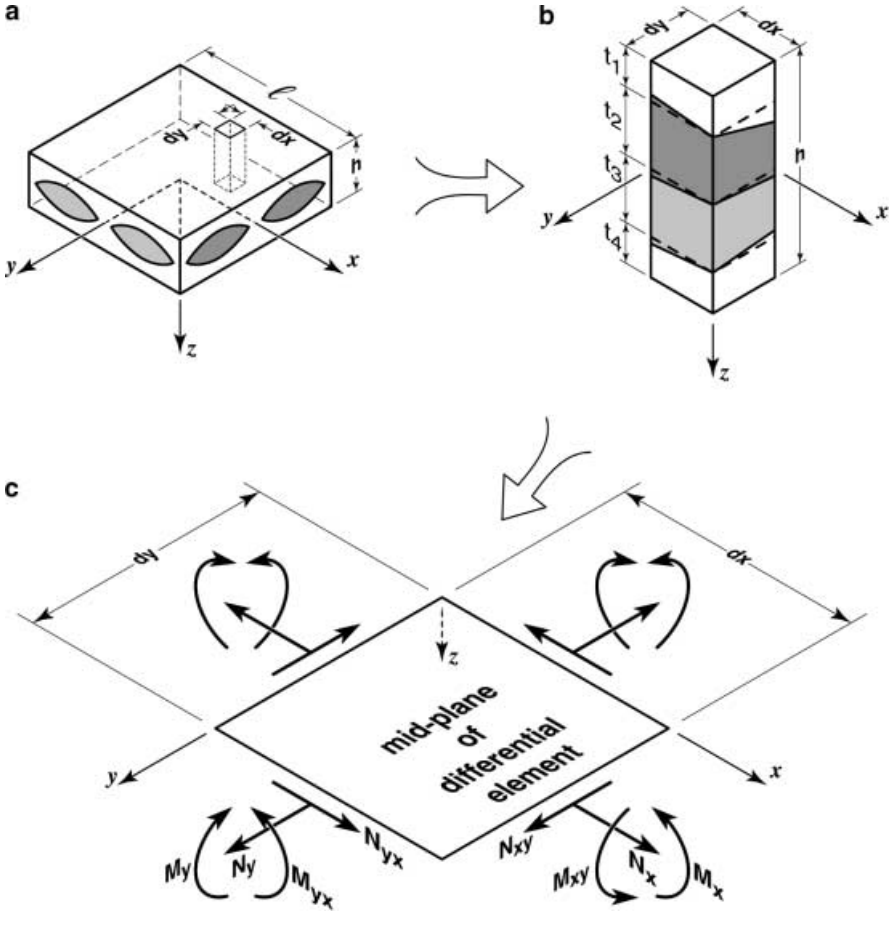

Fig. 4a–c. The 4-layered laminate employed in the modified lamination theory [1]. **a** The woven unit-cell. **b** A differential "column" extracted from the woven unit-cell. **c** The differential column mid-plane used to model the structure as a composite laminate

$$[\bar{N}_x] = \begin{bmatrix} \bar{N}_z^x & \bar{N}_z^y & \bar{N}_z^{\mathrm{sh}} \\ 0 & 0 & 0 \\ 0 & 0 & 0 \end{bmatrix} \tag{20}$$

$$[\bar{N}_y] = \begin{bmatrix} 0 & 0 & 0 \\ \bar{N}_z^x & \bar{N}_z^y & \bar{N}_z^{\mathrm{sh}} \\ 0 & 0 & 0 \end{bmatrix} \tag{21}$$

Through Eq. (18), the three-dimensional micro-displacement fields in the interior of the element have been established in terms of the nodal displacements. The complete micro-strain and micro-stress fields in the interior of the element are formulated in the context of the modified lamination theory in the next section.

2.2 Micro-strains and micro-stresses

Consistent with the modified lamination theory (see [1]), the micro-strains in the interior of the element are given as

$$\begin{Bmatrix} \epsilon_x \\ \epsilon_y \\ \gamma_{xy} \end{Bmatrix} = \begin{Bmatrix} \epsilon_x^0 \\ \epsilon_y^0 \\ \gamma_{xy}^0 \end{Bmatrix} + z \begin{Bmatrix} \kappa_x^0 \\ \kappa_y^0 \\ \kappa_{xy}^0 \end{Bmatrix} \tag{22}$$

where the mid-plane strains $\{\epsilon_x^0, \epsilon_y^0, \gamma_{xy}^0\}$ and the mid-plane curvatures $\{\kappa_x^0, \kappa_y^0, \kappa_{xy}^0\}$ are as follows:

$$\begin{Bmatrix} \epsilon_x^0 \\ \epsilon_y^0 \\ \gamma_{xy}^0 \end{Bmatrix} = \begin{Bmatrix} u_{0,x} \\ v_{0,y} \\ u_{0,y} + v_{0,x} \end{Bmatrix} \text{ and}$$

$$\begin{Bmatrix} \kappa_x^0 \\ \kappa_y^0 \\ \kappa_{xy}^0 \end{Bmatrix} = -\begin{Bmatrix} w_{0,xx} \\ w_{0,yy} \\ 2w_{0,xy} \end{Bmatrix} . \tag{23}$$

Using Eq. (17), the mid-plane strain vector $\{\epsilon^0\}$ can be expressed in terms of the nodal displacement vector $\{u_N\}$ as follows:

$$\begin{aligned} \{\epsilon^0\} &= ([B_0][D]^{-1}[A_0] + [\bar{N}_1][D]^{-1}[A_0]_{,x} \\ &\quad + [\bar{N}_2][D]^{-1}[A_0]_{,y})\{u_N\} \\ &= [B_1]\{u_N\} \end{aligned} \tag{24}$$

where the matrix $[B_0]$ and the auxiliary matrices $[\bar{N}_1]$ and $[\bar{N}_2]$, generated in the wake of partially differentiating the auxiliary matrix $[A_0]$ are:

$$[B_0] = \begin{bmatrix} \bar{N}_{x,x}^x & \bar{N}_{x,x}^y & \bar{N}_{x,x}^{\mathrm{sh}} \\ \bar{N}_{y,y}^x & \bar{N}_{y,y}^y & \bar{N}_{y,y}^{\mathrm{sh}} \\ \bar{N}_{x,y}^x + \bar{N}_{y,x}^x & \bar{N}_{x,y}^y + \bar{N}_{y,x}^y & \bar{N}_{x,y}^{\mathrm{sh}} + \bar{N}_{y,x}^{\mathrm{sh}} \end{bmatrix} , \tag{25}$$

$$[\bar{N}_1] = \begin{bmatrix} \bar{N}_x^x & \bar{N}_x^y & \bar{N}_x^{\mathrm{sh}} \\ 0 & 0 & 0 \\ \bar{N}_y^x & \bar{N}_y^y & \bar{N}_y^{\mathrm{sh}} \end{bmatrix} , \tag{26}$$

$$[\bar{N}_2] = \begin{bmatrix} 0 & 0 & 0 \\ \bar{N}_y^x & \bar{N}_y^y & \bar{N}_y^{\mathrm{sh}} \\ \bar{N}_x^x & \bar{N}_x^y & \bar{N}_x^{\mathrm{sh}} \end{bmatrix} . \tag{27}$$

The mid-plane curvatures $\{\kappa^0\}$ are also given as follows:

$$\begin{aligned} \{\kappa^0\} &= -([C_0][D]^{-1}[A_0] + [\bar{N}_3][D]^{-1}[A_0]_{,x} \\ &\quad + [\bar{N}_4][D]^{-1}[A_0]_{,y})\{u_N\} \\ &= -[C_1]\{u_N\} \end{aligned} \tag{28}$$

where the matrices $[C_0]$, $[\bar{N}_3]$, and $[\bar{N}_4]$ appearing in Eq. (28) are:

$$[C_0] = \begin{bmatrix} \bar{N}_{z,xx}^x & \bar{N}_{z,xx}^y & \bar{N}_{z,xx}^{\mathrm{sh}} \\ \bar{N}_{z,yy}^x & \bar{N}_{z,yy}^y & \bar{N}_{z,yy}^{\mathrm{sh}} \\ 2\bar{N}_{z,xy}^x & 2\bar{N}_{z,xy}^y & 2\bar{N}_{z,xy}^{\mathrm{sh}} \end{bmatrix} , \tag{29}$$

$$[\bar{N}_3] = 2\begin{bmatrix} \bar{N}_{z,x}^x & \bar{N}_{z,x}^y & \bar{N}_{z,x}^{\mathrm{sh}} \\ 0 & 0 & 0 \\ \bar{N}_{z,y}^x & \bar{N}_{z,y}^y & \bar{N}_{z,y}^{\mathrm{sh}} \end{bmatrix} , \tag{30}$$

$$[\bar{N}_4] = 2\begin{bmatrix} 0 & 0 & 0 \\ \bar{N}_{z,y}^x & \bar{N}_{z,y}^y & \bar{N}_{z,y}^{\mathrm{sh}} \\ \bar{N}_{z,x}^x & \bar{N}_{z,x}^y & \bar{N}_{z,x}^{\mathrm{sh}} \end{bmatrix} . \tag{31}$$

Thus, the micro-strains in the interior of the element are expressed in terms of the nodal displacements $\{u_N\}$ as follows:

$$\begin{Bmatrix} \epsilon_x \\ \epsilon_y \\ \gamma_{xy} \end{Bmatrix} = ([B_1] - z[C_1])\{u_N\} = [B]\{u_N\} \tag{32}$$

The micro-stresses of the k-th layer (see Fig. 4b) within the element (or unit-cell) are expressed in terms of the local stiffness of the k-th layer and the associated micro-strains in accordance with the modified laminate theory (see [1]) as follows:

$$\begin{Bmatrix} \sigma_x \\ \sigma_y \\ \tau_{xy} \end{Bmatrix}_k = \begin{bmatrix} \bar{Q}_{11} & \bar{Q}_{12} & 0 \\ \bar{Q}_{12} & \bar{Q}_{22} & 0 \\ 0 & 0 & \bar{Q}_{66} \end{bmatrix}_k \begin{Bmatrix} \epsilon_x \\ \epsilon_y \\ \gamma_{xy} \end{Bmatrix} = [\bar{Q}]_k \begin{Bmatrix} \epsilon_x \\ \epsilon_y \\ \gamma_{xy} \end{Bmatrix} \tag{33}$$

where $[\bar{Q}]_k$ represents the stiffness matrix of the k-th layer.

2.3 Finite element equations

The total potential energy Π of a deformable system is formulated in terms of the total strain energy U and the potential energy of external forces W as follows:

$$\Pi = U - W \tag{34}$$

Here,

$$\begin{aligned} U &= \frac{1}{2}\int_V \{\epsilon\}^T\{\sigma\}\mathrm{d}V \\ W &= \int_{S_T} \{u\}^T\{T\}\mathrm{d}S . \end{aligned} \tag{35}$$

The vector $\{T\}$ and the notation S_T appearing in Eq. (35) represents the traction vector and its traction surface, respectively. With the displacements, micro-strains, and micro-stresses formulated in the preceding sections, the total potential energy Π of Eq. (34) is further expanded as follows:

$$\Pi = \frac{1}{2}\{u_N\}^T \int_V [B]^T[\bar{Q}][B]\mathrm{d}V\{u_N\} - \{u_N\}^T \int_{S_T} [A^T]\{T\}\mathrm{d}S \tag{36}$$

By requiring the minimum total potential energy in the system considered ($\delta\Pi = 0$), the following linear finite element equations are derived:

$$[K]\{u_N\} = \{f_N\} \tag{37}$$

where the stiffness matrix $[K]$ and force vector $\{f_N\}$ assume the classical form as follows:

$$[K] = \int_V [B]^T[\bar{Q}][B]\mathrm{d}V \quad \Leftarrow \text{ Global stiffness matrix}$$
$$\{f_N\} = \int_{S_T} [A]^T\{T\}\mathrm{d}S \quad \Leftarrow \text{ Global force vector} \tag{38}$$

Consistent with the conventional finite element formulation, the volume integral used in obtaining the global stiffness matrix $[K]$ in Eq. (38) above is evaluated within each element and assembled over the domain V as follows:

$$[K] = \sum_{e=1}^{N_{el}} [K]_e \tag{39}$$

where the element stiffness matrix $[K]_e$ is now given through an element volume integration as follows:

$$[K]_e = \int_{V_e} [B]_e^T[\bar{Q}]_e[B]_e\mathrm{d}V_e \tag{40}$$

Further expanding Eq. (38), the element stiffness matrix takes a final form as a combination of three individual matrices, which are related to the extensional, coupling, and bending contribution, respectively, as follows:

$$[K] = \int_V [B_1]^T[\bar{Q}][B_1][A_0]\mathrm{d}V - \int_V z[B_1]^T[\bar{Q}][C_1]\mathrm{d}V - \int_V z[C_1]^T[\bar{Q}][B_1]\mathrm{d}V + \int_V z^2[C_1]^T[\bar{Q}][C_1]\mathrm{d}V$$
$$= [K]_e + [K]_c + [K]_c^T + [K]_b \tag{41}$$

The subscripts 'e', 'c', and 'b' found in Eq. (41) are used to represent the extensional, coupling, and bending contribution of each corresponding matrix. It is important to note that the matrices $[K]_e$, $[K]_c$, and $[K]_b$ are analogous to the matrices appearing in the laminate constitutive equations conventionally denoted by $[A]$, $[B]$, and $[D]$ in the modified lamination theory (see [1]).

The boundary surfaces where the force vector shall be integrated are presented in Fig. 5. It is worthwhile to note that this element can account not only for in-plane loading but also for flexural loading consistent with Fig. 5. The expanded form of the force vector is as follows:

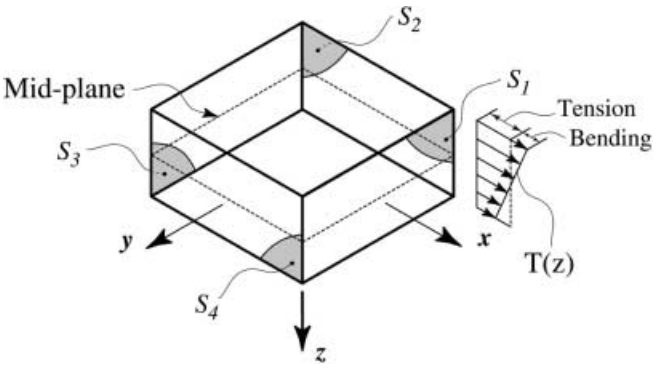

Fig. 5. Four boundary surfaces on which the force vector is evaluated

$$\{f_N\} = \int_{S_1} [A]^T\{T\}\mathrm{d}S + \int_{S_2} [A]^T\{T\}\mathrm{d}S + \int_{S_3} [A]^T\{T\}\mathrm{d}S + \int_{S_4} [A]^T\{T\}\mathrm{d}S \tag{42}$$

Although a more elaborate form for the nodal force vector $\{f_N\}$ can be obtained using Eq. (18), it is not presented in this paper. The element proposed in this work is also capable of accounting for non-linearities induced by the degradation of material properties resulting from the evolution of stress-induced damage in micro-constituents of the system. As such, both the stiffness matrix and the force vector, when accounting for residual dilatational effects, may be functions of the displacement fields as follows:

$$K(\{u_N\}_{r-1})]\{u_N\}_r = \{f_N(\{u_N\}_{r-1})\} \tag{43}$$

Non-linearities of the type incorporated in the above finite element equations can be treated numerically using an iterative scheme, wherein the stiffness matrix and the force vector are updated recursively with the preceding solution set $\{u_N\}_{r-1}$ and used to obtain the current solution set $\{u_N\}_r$.

2.4 Stiffness integration scheme

For the accurate evaluation of the stiffness matrix and force vector, the Gauss-Legendre integration scheme is employed. Eight isoparametric domain elements as shown in Fig. 6a are introduced as needed to model the pre-existing void of a typical woven CMC unit-cell as discussed in [1]. Within each domain element, a user-controlled $M \times N$ Gauss integration station is used, consistent with the Rayleigh–Ritz method convergence studies reported in [1]. A user-controlled n_z Gauss integration station is also introduced at each point of the $M \times N$ Gauss integration station, as shown in Fig. 6b, for the stiffness evaluation in the thickness z-direction appearing equation (41). As a result, a total of $8 \times M \times N \times n_z$ Gauss integration points are used to evaluate the stiffness matrix and a total of $8 \times M \times N$ number of Gauss integration points are used for the force vector.

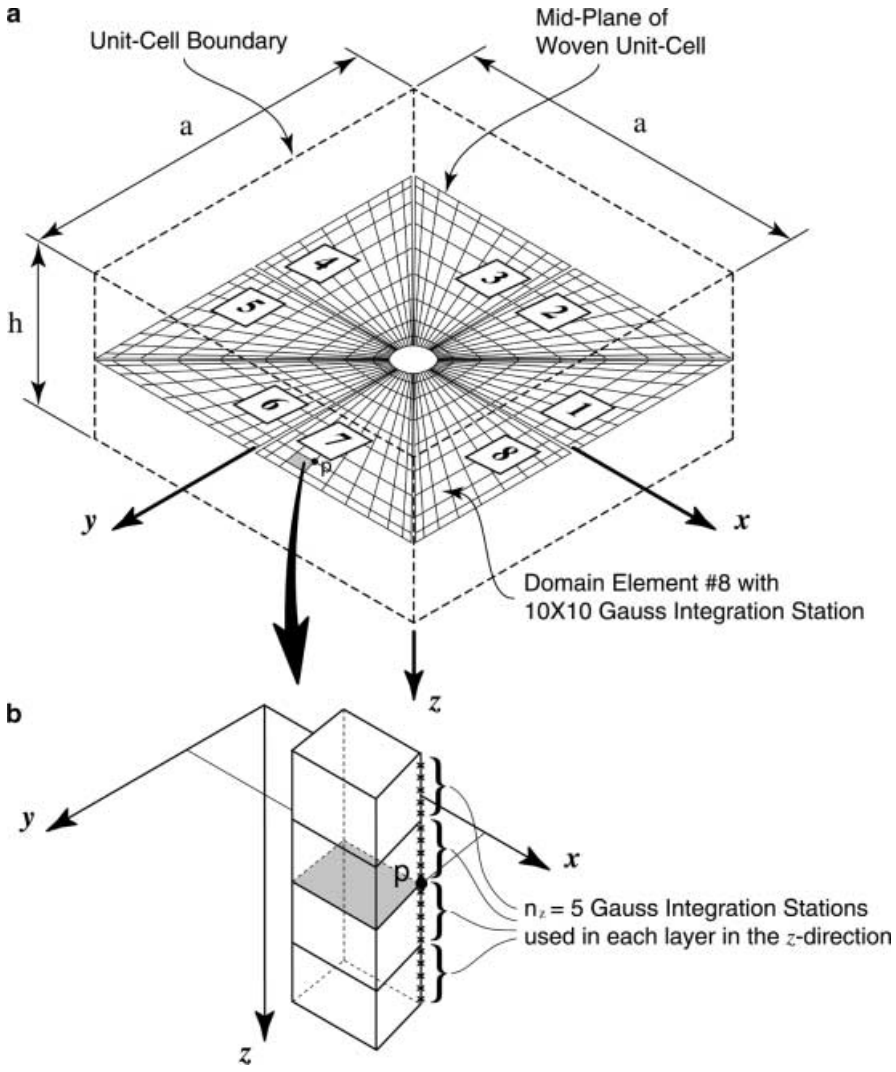

Fig. 6a, b. a The x–y grid of Gauss integration stations used in the calculation of the volume integrals of the Rayleigh–Ritz method developed in [1]. **b** Integration in the out-of-plane z-direction is carried out using a user-controlled n_z number of Gauss points within each layer as shown above

3
Element performance

The element performance is demonstrated through an uniaxial tension and asymptotic near-tip boundary value problems for a cracked plain weave composite. By considering a simple problem such as the uniaxial tension case, we will demonstrate the specialized element's unique capability of capturing micro-stress fields within the interior of the element. However, the emphasis of this section is placed on the near-tip crack studies, where we will address various aspects of the proposed element.

3.1
Uniaxial tension problem

As shown in Fig. 7, an uniaxial tension specimen of dimensions $2L \times 2H$ was discretized using the specialized element. Appropriate symmetric conditions and uniform displacement boundary conditions ($u = U_x$ for all the nodes at the boundary) were enforced. The resulting finite element mesh and its deformed configuration are shown in Fig. 7b.

Geometry and unit-cell size effects were explored by either changing the macroscopic specimen dimension L and H or by changing the unit-cell size a while keeping the

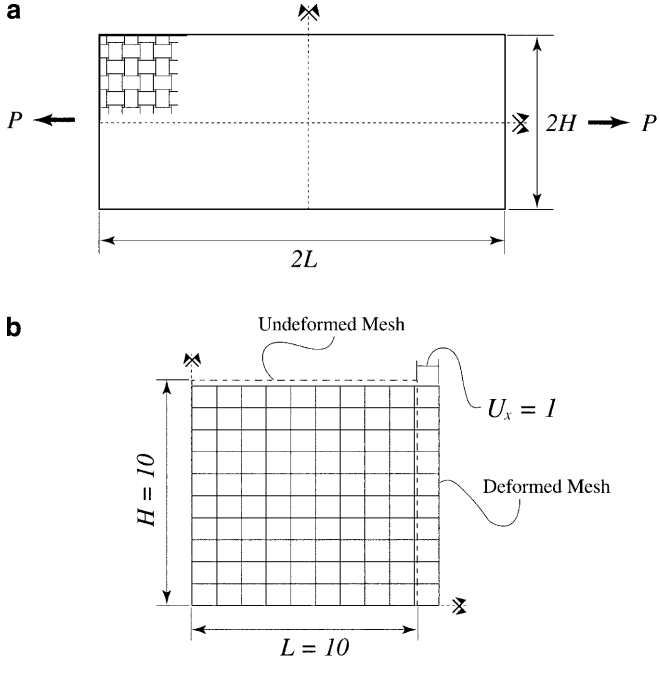

Fig. 7a, b. a An uniaxial tension specimen. **b** The finite element mesh and deformed configuration

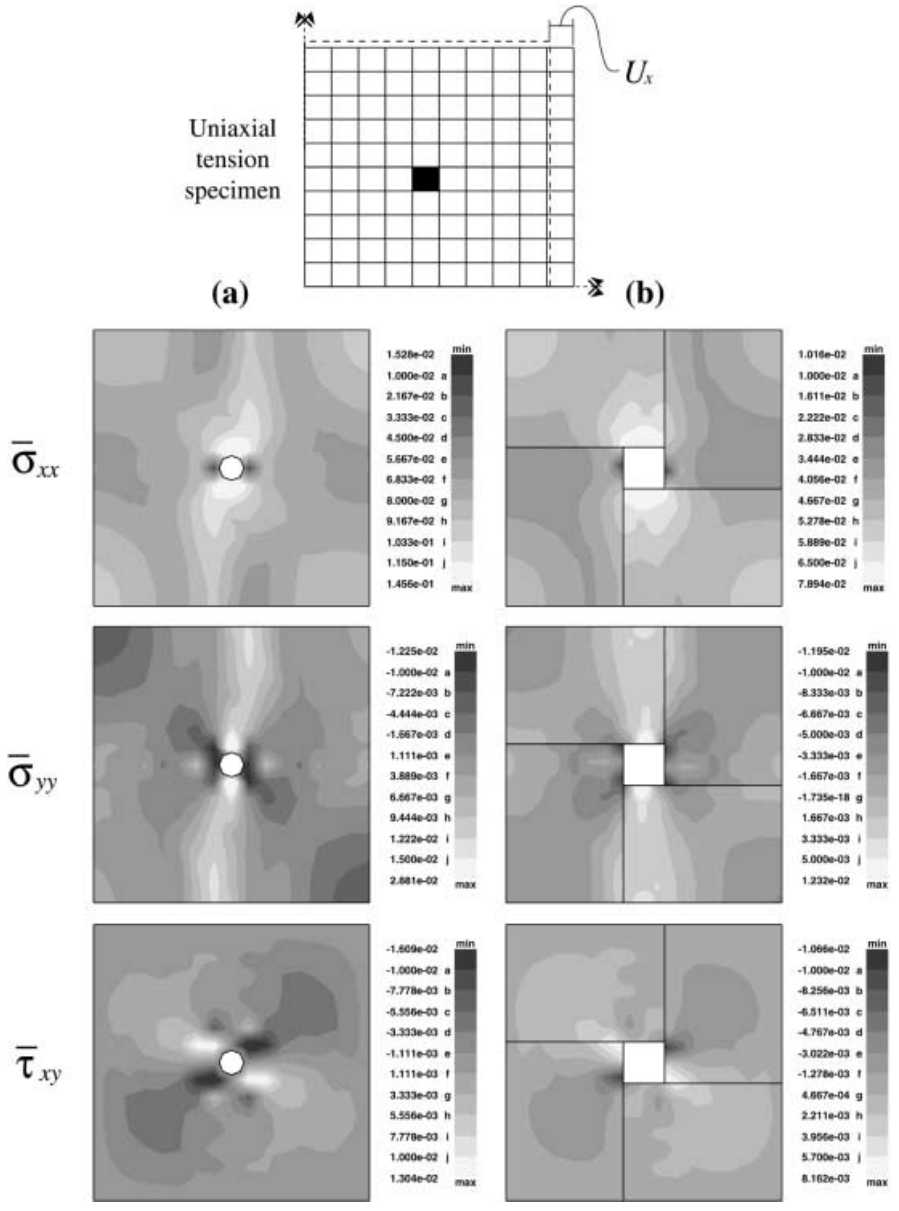

Fig. 8a, b. a The micro-stresses $\bar{\sigma}_{xx}$, $\bar{\sigma}_{yy}$, and $\bar{\tau}_{xy}$ obtained at the matrix phase. **b** The micro-stresses obtained at the tow phases

specimen dimension constant. The finite element nodal displacements along the neutral axis were monitored for each solution and were compared to analytical solutions obtained for a self-similar homogeneous specimen by using a discrete L_2 norm. In all cases considered, the finite element solutions obtained using the specialized element yielded extremely small relative percent errors of less than 10^{-5}%.

The micro-stress fields obtained from the uniaxial tension case are presented in Fig. 8. As indicated in the above figure, the stresses were obtained at the element marked with black filling. The results in column (a) of Fig. 8 represent the stresses obtained in the matrix phase and those in column (b) represent the stresses in the tow phases. As shown in the above figure, stress concentration regions are predicted in the vicinity of the hole for both the normal micro-stress components $\bar{\sigma}_{xx}$ and $\bar{\sigma}_{yy}$. The formation of a stress concentration band perpendicular to the loading direction emanating from the void at the center of the unit-cell is also predicted consistent with the 3-D finite element prediction reported in [21]. It is evident from Fig. 8 that even though each element is subjected to macroscopic uniform tension, spatially varying micro-stresses are predicted within each element consistent with the woven micro-structural characteristics. Also, the contours for the shear stress component $\bar{\tau}_{xy}$ for both phases clearly demonstrate the existence of non-trivial micro-shear stress induced by the micro-structure of the woven system. It is of importance to note that the micro-stresses results presented in Fig. 8 compare favorably to the 3-D finite element results reported in [21].

3.2
Near-tip crack problems

In accordance with other similar asymptotic near-tip studies, a rectangular domain of dimensions $2R \times 2R$ containing the tip of an otherwise planar crack at its

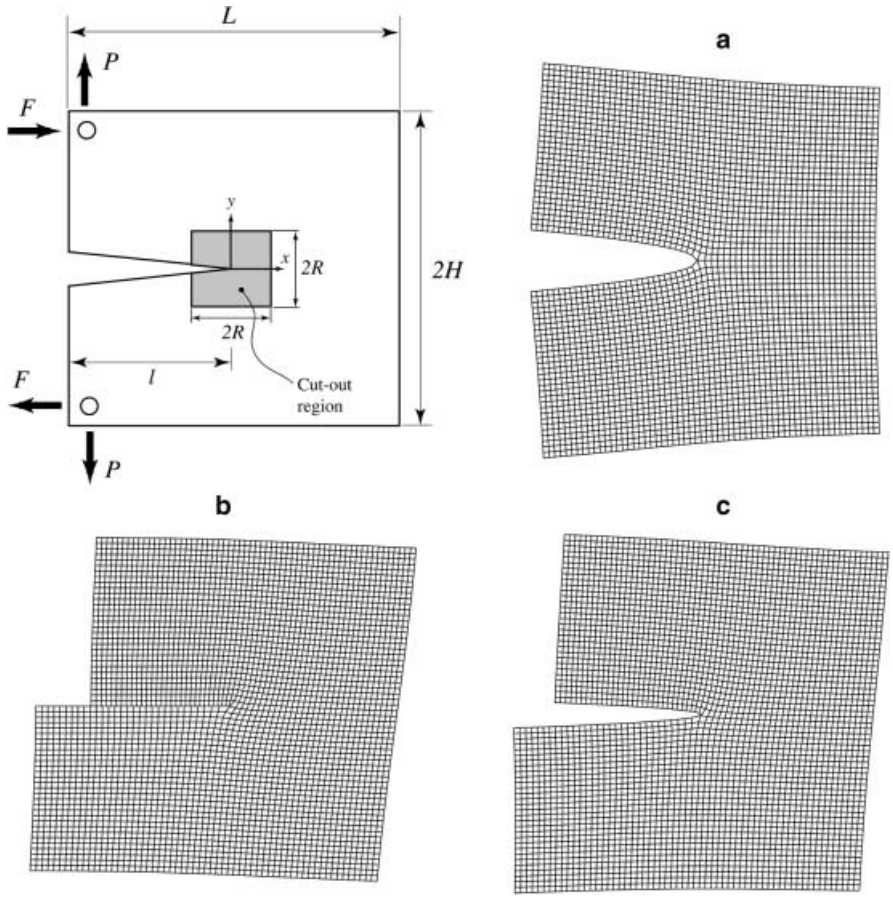

Fig. 9a–c. Asymptotic neat-tip studies are performed using a cut-out region of dimension $2R \times 2R$ close to the crack-tip. The magnified deformed meshes shown above were obtained by applying the homogeneous displacements along the cut-out boundary for **a** mode-I loading. **b** mode-II loading and **c** mixed mode loading with $K_{\mathrm{I}}^0 = K_{\mathrm{II}}^0$

center, is extracted from a finite geometry such as the compact tension specimen as shown in Fig. 9. It is well understood that the entire extracted region is embedded well within the K-dominated field. As such, any in-plane loading applied to the finite specimen will induce mode-I, mode-II or any combination of the above (known as mixed mode) conditions, at the crack-tip. In this study, three near-tip loading cases are considered: mode-I and mode-II applied individually, and mixed mode loading conditions with equal amounts of mode-I and mode-II present. In each of the above cases, the known K-fields obtained for elastic homogeneous orthotropic systems are applied along the boundary of the cut-out region. Traction-free crack surface conditions are also enforced. The boundary displacements imposed (as discussed above), are calculated using the effective (homogenized) elastic properties associated with the woven microstructure considered in the study. Such properties are easily obtained from unit-cell studies as discussed elsewhere [16, 20]. As the cell-size $a \to 0$, the composite materials behave like homogeneous orthotropic materials with these effective properties in the limit (see e.g. [22–24] for more on homogenization of periodic materials).

The interior of the cut-out region is discretized with the specialized element developed in this study (see Fig. 9). The number of elements as well as their locations in the considered domain are automatically determined in accordance with the actual lay-out of the composite mat in the cut-out domain, since each element exactly matches the symmetric woven unit-cell as shown in Fig. 2. Clearly, this imposes certain restrictions on the number of elements to be used (since we always have mesh-size $h =$ cell-size a). In light of the above, it is assumed that a sufficient number of unit-cells exist in the near-tip domain in this study. It is important to note that with a given domain (problem) size, different meshes may represent different unit-cell microstructures and thus, different material systems. As $a = h \to 0$, the effective properties of the material asymptotically approach the effective (homogenized) limit. These materials are all related in the sense that as the unit-cell size $a \to 0$, the materials behave like the homogenized orthotropic material in the limit. We refer to [22–24] and the references therein for more on homogenization of periodic materials. Although analytical solutions for $a > 0$ are not available for the problems considered in this study, such solutions are available for the limiting (homogenized) orthotropic materials (the '$a = 0$' case).

As a test of our specialized element, we therefore investigate whether the computed mid-plane displacements for $a > 0$ converge to the analytical ones ($a = 0$) when the cell-size a is decreased. We investigate the order of observed convergence as well, by comparing it to that obtained when the limiting orthotropic problem is discretized by the 4-noded isoparametric plane elasticity element, using a grid of mesh-size h. Also, the proposed element's unique capability of effectively predicting the micro-stresses in the interior of its microstructure is

Table 1. Micro-structural, mesoscopic, and unit-cell properties characteristic of a CVI ceramic matrix plain weave fabric composite. The listed properties were obtained using the hierarchical micromechanics model developed in [16, 20]

(a) Microstructural input parameters

Fiber	Fiber coating	Matrix	Bundle coating	Volume fractions	Geometry
$\hat{E}_f = 0.5$ $\nu_f = 0.2$	$\hat{E}_{fc} = 0.125$ $\nu_{fc} = 0.25$	$\hat{E}_m = 1.0$ $\nu_m = 0.3$	$\hat{E}_{bc} = 0.25$ $\nu_{bc} = 0.25$	$C_f = 0.5$ $C_{fc} = 0.05$ $C_{bm} = 0.1$ $C_{bp} = 0.15$ $C_{bc} = 0.20$ $C_m = 1.0$ $C_{mp} = 0.0$	$\hat{a} = 1.0$ $\hat{b} = 0.1$ $\hat{g} = 0.15$ $\hat{h} = 0.2$ $\hat{l} = 1.0$ $\hat{t} = 0.03$

(b) Meso- and macro-scopic output

	Effective tow	Effective matrix	Overall volume fractions	Undamage unit-cell
	$\hat{E}_{11} = 0.346$ $\hat{E}^{\ell}_{22} = 0.285$ $\hat{G}_{12} = 0.119$ $\hat{G}^{\ell}_{23} = 0.115$ $\nu_{12} = 0.219$ $\nu^{\ell}_{23} = 0.234$	$\hat{E}_{\bar{m}} = 0.1$ $\hat{G}_{\bar{m}} = 0.385$ $\nu_{\bar{m}} = 0.3$	$V_{\text{fill}} = 0.272$ $V_{\text{warp}} = 0.272$ $V_{\text{matrix}} = 0.251$ $V_{\text{void}} = 0.204$	$\hat{E}_x = 0.413$ $\hat{E}_y = 0.413$ $\nu_{xy} = 0.261$ $\nu_{yx} = 0.261$ $\hat{G}_{xy} = 0.159$

presented through macro-stress and micro-stress contours obtained from the mode-I crack problem. Finally, the characteristics of the homogeneous mid-plane strain vector $\{\bar{\epsilon}^h_{xx}, \bar{\epsilon}^h_{yy}, \bar{\tau}^h_{xy},\}$ are investigated to facilitate effective numerical alternatives to the specialized finite element proposed here.

The normalized material and geometry parameters representing the plain weave composite used in this study are listed in Table 1a. The material parameters are normalized with the modulus of elasticity of the matrix E_m and the geometric parameters are normalized with the unit-cell length a. The meso-scopic effective (or homogenized) tow and inter-tow matrix elastic properties are listed in Table 1b. The unit-cell volume fractions occupied by the meso-scopic phases are listed in the third column of the table. Effective elastic properties of the unit-cell are listed in the last column of the table.

3.2.1 Cell size convergence

In this section, we investigate the numerical convergence displayed by our specialized element as the cell-size a (taken equal to the mesh-size h) tends to 0. Since we know that the exact solution u^{ex}_a tends to the (known) analytical solution (using effective orthotropic properties) $u^{\text{eff}}(= u^{\text{ex}}_0)$ as $a \to 0$, we expect that the approximate (specialized element) solution u^{sp}_0 should also converge to u^{eff} (as $a \to 0$), if our element is accurate. We show this is, in fact, the case. Let us note that this is very similar to the phenomenon of h-convergence in finite elements, since as we decrease $a(= h)$ for a fixed domain, the number of degrees of freedom $N_{\text{dof}} = \text{O}(a^{-2}) = \text{O}(h^{-2})$ increases. In fact, we demonstrate that the observed order of convergence in the norm (see Eq. (44)) below with the specialized element is the same as that obtained when the 4-noded isoparametric element is used to obtain an approximate solution u^{fe}_h to u^{eff} (and $h \to 0$).

We performed this test with the crack problem under mode-I, mode-II, and mixed mode ($K^0_I = K^0_{II}$) loading conditions (Fig. 9). A semi-infinite crack is embedded in an otherwise infinite woven composite (see Fig. 9a) and a cut-out region indicated by the dashed lines surrounding the physical crack-tip is considered for a finite element model. As discussed above, homogeneous displacement boundary conditions are imposed at the boundary of the near-tip domain to simulate each loading condition, as shown in Fig. 9a. The spatial distances are normalized with the reference length a and the stresses are normalized with the reference stress $\sigma_0 = |K^0|/\sqrt{2\pi R}(R/a)$, while the displacements are normalized with $U_0 = |K^0|/E_m\sqrt{R/2\pi}$. The magnified deformed mesh for mode-I, mode-II, and mixed mode is presented in Fig. 9a–c, respectively.

Accuracy is assessed by calculating the relative percent error.

$$E(u^{\text{eff}} - u^{\text{sp}}_a) = \frac{\|u^{\text{eff}} - u^{\text{sp}}_a\|}{\|u^{\text{eff}}\|} \times 100\% \tag{44}$$

where

$$\|u\| = \left[\sum_{i=1}^{N_{\text{dof}}} u_i^2\right]^{1/2}, \tag{45}$$

and u^{eff}, u^{sp}_a represent mid-plane displacements. For comparison purposes, the relative percent error, $E(u^{\text{eff}} - u^{\text{fe}}_h)$ is also plotted on the same plot. Results obtained for all three loading cases considered, are presented in Fig. 10. A log–log scale was used for each plot.

We notice, first of all, that the errors in Fig. 10 are all decreasing as $N_{\text{dof}} \to \infty$, and the observed convergence is $\text{O}(N^{-1/2}_{\text{dof}})$ in all cases. For the finite error $u^{\text{eff}} - u^{\text{fe}}_h$, this translates to $\text{O}(h)$ convergence. Noting that the norm (Eq. (44)) is essentially a discrete L_2 norm, this is exactly the rate of convergence expected theoretically for a crack

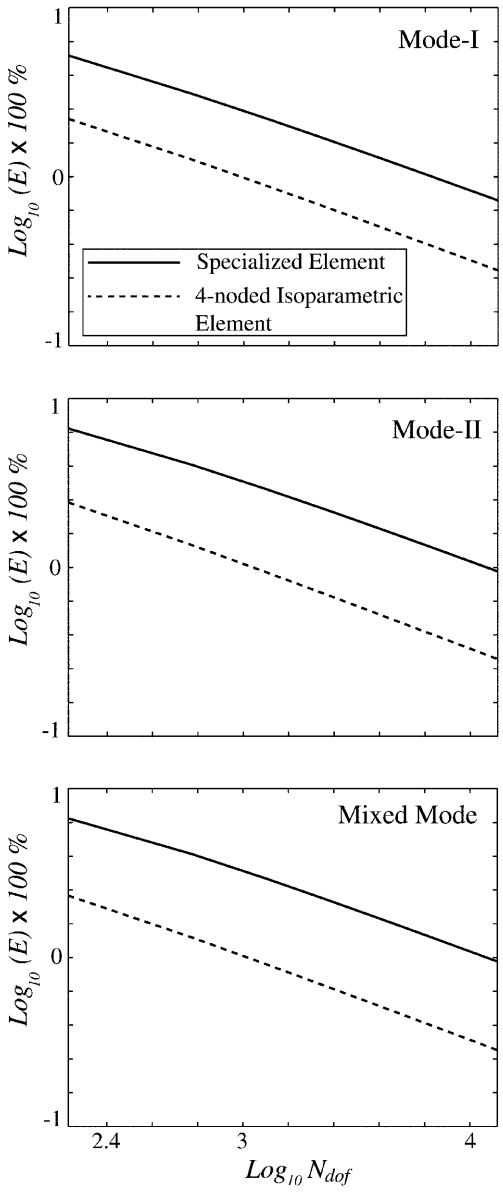

Fig. 10. The relative errors in the nodal displacements associated with the specialized element (solid lines) and the 4-noded isoparametric element (dashed lines) are plotted against the corresponding number of degrees of freedom N_{dof} in a log–log scale

problem (see [25]) with the 4-noded isoparametric element.

To analyze the error in the specialized element, we write

$$u^{\text{eff}} - u_a^{\text{sp}} = (u^{\text{eff}} - u_a^{\text{ex}}) + (u_a^{\text{ex}} - u_a^{\text{sp}}) \tag{46}$$

Since $u^{\text{eff}} \equiv u_0^{\text{ex}}$, the first component in Eq. (46) is the error due to homogenization. Following the theory developed for model problems (see [22]), this may be expected to be an $O(a)$ in the L_2 norm, i.e. $O(N_{\text{dof}}^{-1/2})$. Using this estimate in Eq. (46) together with the triangle inequality, then it can be shown that $\|u_a^{\text{ex}} - u_a^{\text{sp}}\|$ is also $O(N_{\text{dof}}^{-1/2}) = O(a) = O(h)$, which, by the results in [25] is again the best that can be expected. Hence, the observed results in Fig. 10 suggest that the specialized element is optimally convergent in the norm (Eq. (44)), and that our numerical scheme is sound.

Table 2. The relative errors obtained for $N_{\text{dof}} = 13202$ for each loading case reported in Fig. 10

	Mode-I (%)	Mode-II (%)	Mixed mode (%)
Specialized element	0.72	0.95	0.95
4-Noded isoparametric element	0.28	0.29	0.28

Let us remark on a further observation from Fig. 10. It is seen that the error curves for the specialized element are parallel to, but shifted upwards compared to, the error with the 4-noded isoparametric element. One might be led to conclude, therefore, that the performance of the specialized element is inferior to that of the 4-noded isoparametric element. However, this reasoning is erroneous, because of the simple fact that it is u_a^{ex} that we are really interested in calculating, not the homogeneous limit $u_0^{\text{ex}} (= u^{\text{eff}})$. In other words, the true error is $u_a^{\text{ex}} - u_a^{\text{sp}}$, and we measure $u^{\text{eff}} - u_a^{\text{sp}}$ instead only because u_a^{ex} is not available. In fact, we can expect u_a^{sp} to be closer to the desired solution u_a^{ex} than u_h^{fe} is to u_a^{ex}. The shift in the error curves can be thought of as arising from the error due to homogenization, $u^{\text{eff}} - u_a^{\text{ex}}$ in Eq. (46). Let us mention, though, that as Table 2 shows, the relative error even for $u^{\text{eff}} - u_a^{\text{sp}}$ is less than 1% for $N_{\text{dof}} = 13202$ for each of the problems considered.

3.2.2 Near-tip micro-fields

One of the most important features of the element developed in this study is its ability to capture the local micro-stress fields of woven composites, which are crucial ingredients for establishing a complete mechanical response of such systems. In the mode-I crack problem, for example, even though the 4-noded isoparametric element predicted the mid-plane displacements with a greater accuracy, it is obvious that its solutions are valid only for the homogenized effective woven system. However, the proposed element makes it possible, for the first time, to fully investigate the local micro-stress fields of woven composites by incorporating the unit-cell geometry, the semi-analytical technique of Kuhn et al. [1] and the modified lamination theory in the element formulation.

For reference and comparison purposes, the analytically obtained elastic homogeneous singular stress fields, $\bar{\sigma}_{xx}$, $\bar{\sigma}_{yy}$, and $\bar{\tau}_{xy}$, for the mode-I loading case are presented in Fig. 11a. As discussed earlier, the above results are not new and have been established analytically in [26]. To assess the performance and capabilities of the new specialized element for woven systems, the stress contours for the same loading case obtained via the specialized element are presented in Fig. 11b. It is important to note that the stress contours presented in Fig. 11b represent the effective mid-plane stresses and, as such, they are directly comparable to their analytical counterparts presented in Fig. 11a. To

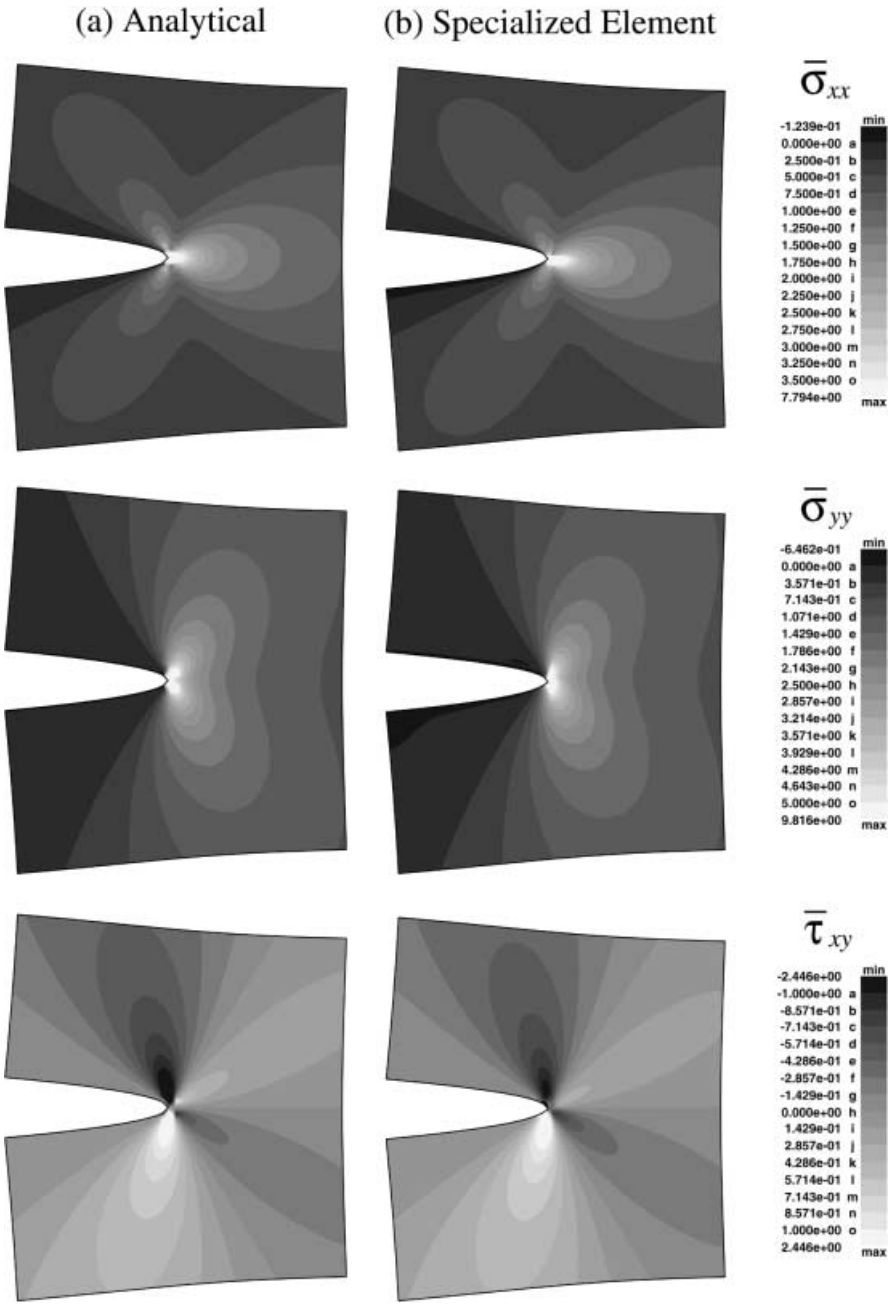

Fig. 11a, b. a The analytically obtained elastic homogeneous singular stress fields, for the mode-I loading case. **b** The effective mid-plane stresses predicted with the specialized element for the same case

obtain such mid-plane stress estimates, the mid-plane strains were obtained from a finite element solution via Eq. (24) (or Eq. (32)), and then the desired mid-plane stress estimates were obtained through Eq. (33) using the effective stiffness of a considered woven system instead of the local stiffness $(\bar{Q}_{ij})_k$. As shown in Fig. 11b, the stresses obtained via the specialized element are remarkably close to their analytical counterparts presented in Fig. 11a. Deviations between the two results appear to exist in a confined annular region along the boundary. Such deviations, however, are to be expected, since the above region is a transition zone between the homogeneous fields applied at the boundary and the elastic micro-fields developed consistent with the discrete microstructure away from the boundary. Apparent micro-deviations of the two results at the immediate vicinity of the crack-tip are also expected due to the singular characteristic of the given elastic fields, which may not be fully captured within the first ring of elements from the crack-tip. The finite element results for the other two loading cases, i.e. mode-II and mixed mode conditions, which are not reported herein, also were observed to be in good agreement with their analytical counterparts.

In addition to obtaining the effective stress estimates such as those presented in Fig. 11b, the specialized element can also provide micro-stress estimates away from the mid-plane at any point within the element via Eq. (33) wherein the local stiffness $(\bar{Q}_{ij})_k$ is used. Such micro-stress results obtained within a small sampling zone (see the top of Fig. 12) containing the crack-tip, are presented in Fig. 12.

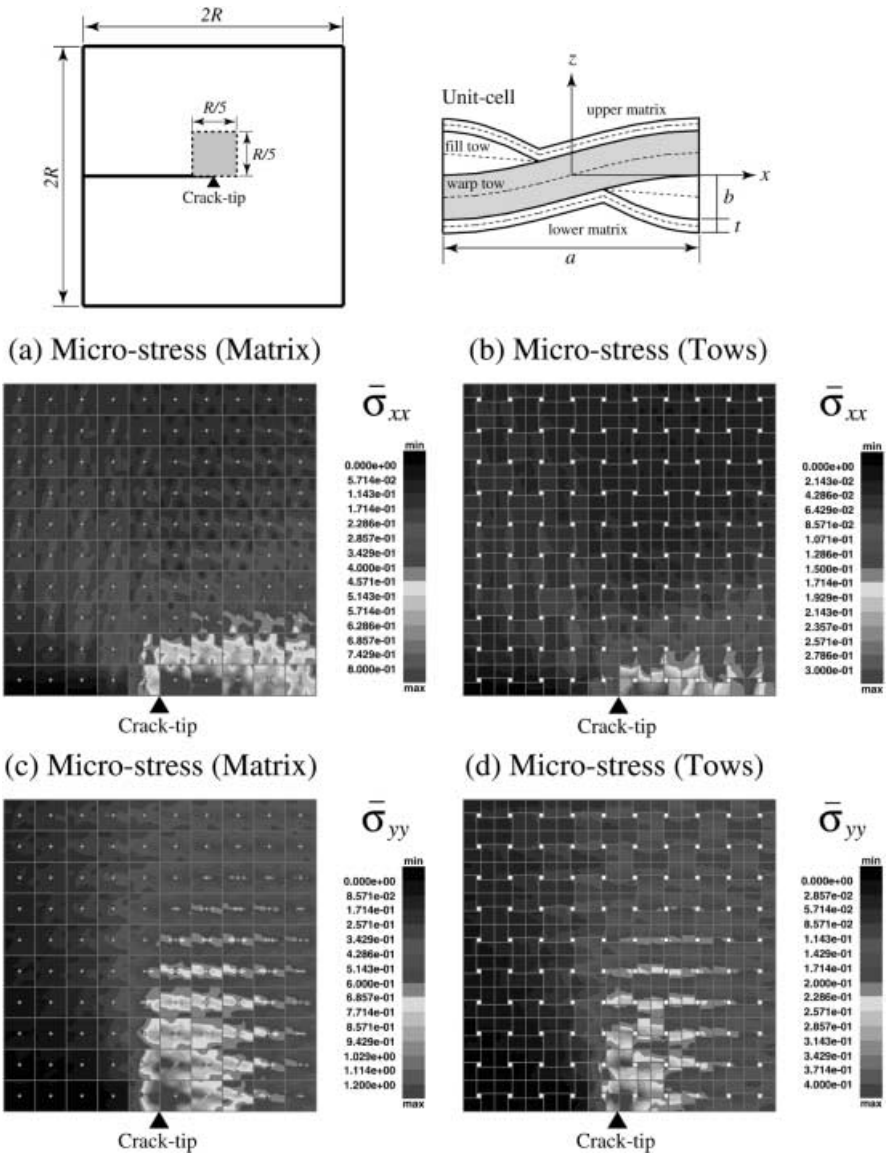

Fig. 12a–d. The mode-I micro-stresses dominating the matrix and tow phases in the immediate crack-tip region. **a** The matrix micro-stress $\bar{\sigma}_{xx}$. **b** The tow micro-stress $\bar{\sigma}_{xx}$. **c** The matrix micro-stress $\bar{\sigma}_{yy}$. **d** The tow micro-stress $\bar{\sigma}_{yy}$

The micro-stress components $\bar{\sigma}_{xx}$, $\bar{\sigma}_{yy}$ for mode-I loading case are reported in the above figure. As shown in the schematic on the top of Fig. 12, the reported micro-stresses were extracted along the mid-surface of the upper matrix layer (see Fig. 12a and c) and those of the fill/warp tows (see Fig. 12b and d). Sufficient data points were included within each element as needed to adequately capture the detailed micro-stress distribution within each element. In contrast to the smooth contour distribution exhibited by the effective mid-plane stresses presented in Fig. 11a and b, the micro-stresses presented in Fig. 12 exhibit an overall texture induced by the heterogeneous microstructure. Micro-bands of stress concentration are shown to exist around the large void within each unit-cell (see Fig. 12a and c). The orientation of each band is shown to slightly vary with the position of the individual unit-cell relative to the crack-tip and observed to be normal to the stress directions.

Such results may have direct implications to the process of microcracking formation, damage evolution and eventual fracture of woven composites. While the matrix micro-stresses are shown to concentrate around the matrix voids, alternating high and low micro-stresses indicating the existence of local micro-bending, are shown to dominate both the fill and warp tows (see Fig. 12b and d). These results highlight the strong performance as well as the potential of the specialized element developed in this study, for example, in obtaining sensible micro-stress measures needed for damage initiation and evolution studies aimed at establishing the non-linear mechanical response and failure characteristics of CMCs.

3.2.3
Homogeneous mid-plane strains

In Fig. 13, the contours for the analytical strain vector $\epsilon^{\text{eff}} = \{\bar{\epsilon}^0_x, \bar{\epsilon}^0_y, \bar{\gamma}^0_{xy}\}$ for the mode-I loading case are presented along with the contours for $\epsilon^{\text{sp}}_a = \{\bar{\epsilon}^h_x, \bar{\epsilon}^0_h, \bar{\gamma}^h_{xy}\}$ for the same loading case, with a taken to be $R/40$. The two are observed to be practically identical, except in the transient and crack-tip regions as discussed earlier.

A more exact comparison is obtained by calculating the difference between the two quantities in an appropriate norm. This time, instead of Eqs. (44) and (45), we use

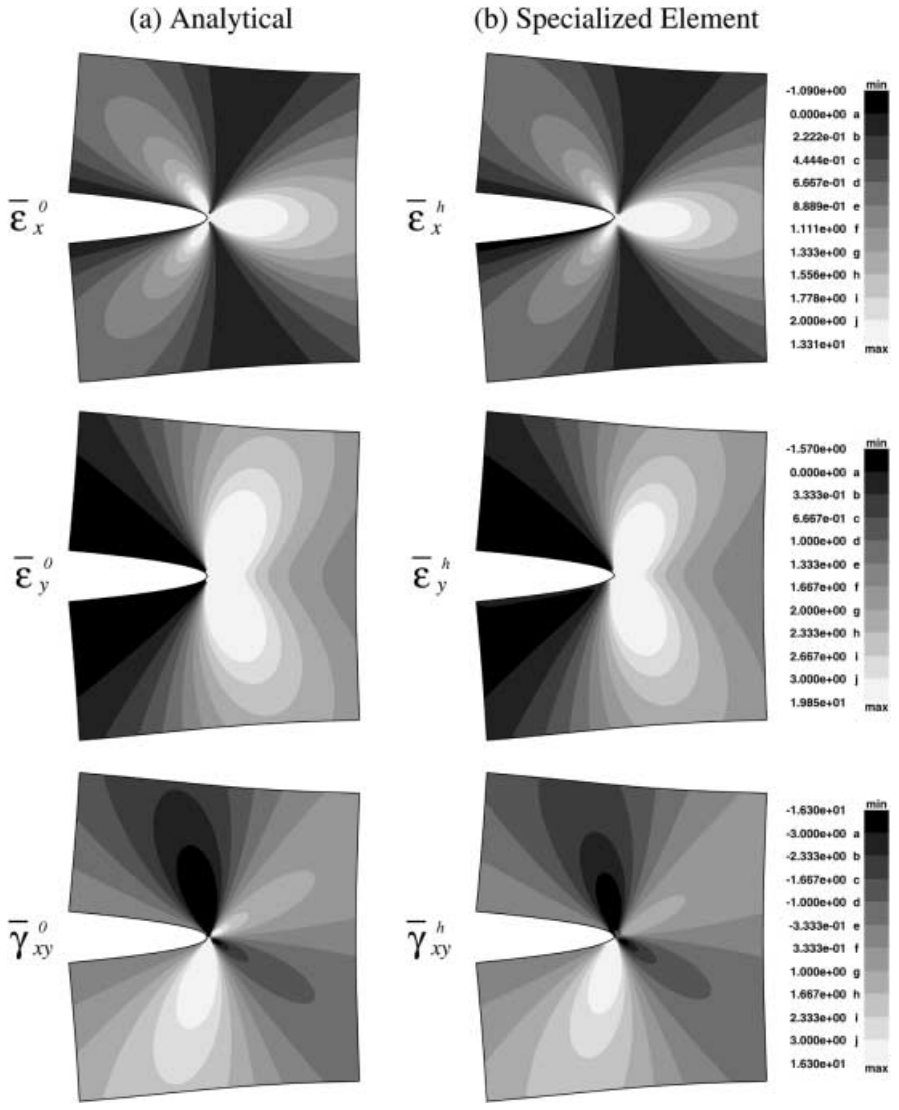

Fig. 13. The analytically obtained homogeneous mid-plane strains $\bar{\epsilon}_x^0$, $\bar{\epsilon}_y^0$, and $\bar{\gamma}_{xy}^0$ and those associated with the specialized element for the mode-I loading case

$$E(\epsilon^{\text{eff}} - \epsilon_a^{\text{sp}}) = \frac{\|\epsilon^{\text{eff}} - \epsilon_a^{\text{sp}}\|}{\|\epsilon^{\text{eff}}\|} \times 100\% \tag{47}$$

where

$$\|\epsilon\| = \left[\sum_{i=1}^{N_{\text{dof}}} \epsilon_{x,i}^2 + \epsilon_{y,i}^2 + \gamma_{xy,i}^2\right]^{1/2}, \tag{48}$$

and the summation is performed upon four Gaussian integration stations on each element of the domain. Figure 14 shows these error plots for various a, i.e., for various N_{dof}, in a log–log scale. Once again, the error $E(\epsilon^{\text{eff}} - \epsilon_h^{\text{fe}})$ with the 4-noded isoparametric element is also plotted for comparison.

It is observed that the isoparametric error decreases at the rate of $N_{\text{dof}}^{-1/4}$ for all three loading cases, which corresponds to an $\text{O}(h^{1/2})$ convergence rate. This is once again optimal for a crack problem when the norm of Eq. (47) (which is a discrete H^1 norm) is used (see e.g. [25]). Moreover, we see that $E(\epsilon^{\text{eff}} - \epsilon_a^{\text{sp}})$ also decreases at the same rate as $E(\epsilon^{\text{eff}} - \epsilon_h^{\text{fe}})$. This shows that for our purposes, we can conclude that the homogeneous mid-plane strains and the normalized deformation vector are close enough in terms of engineering accuracy.

This finding has broad implications, since analytical and numerical finite element solutions for a wide range of homogenized problems may exist or may be readily obtainable. Thus, the homogeneous mid-plane strains obtained through such available solution techniques may be used in conjunction with the current specialized element (via Eq. (13)) to predict the related micro-stress and micro-strain fields dominating heterogeneous composite systems with complex microstructures. Such numerical alternatives are indeed being developed as a result of this study.

While this section presents a wide range of examples on the accuracy and efficiency of the proposed element, there still is a need to compare predictions from the specialized element to those obtained from 3-D finite element analysis to help establish more direct element performance characteristics. Currently, due to the numerical enormity of solving a finite woven geometry using 3-D finite element schemes, such comparisons have not been attempted.

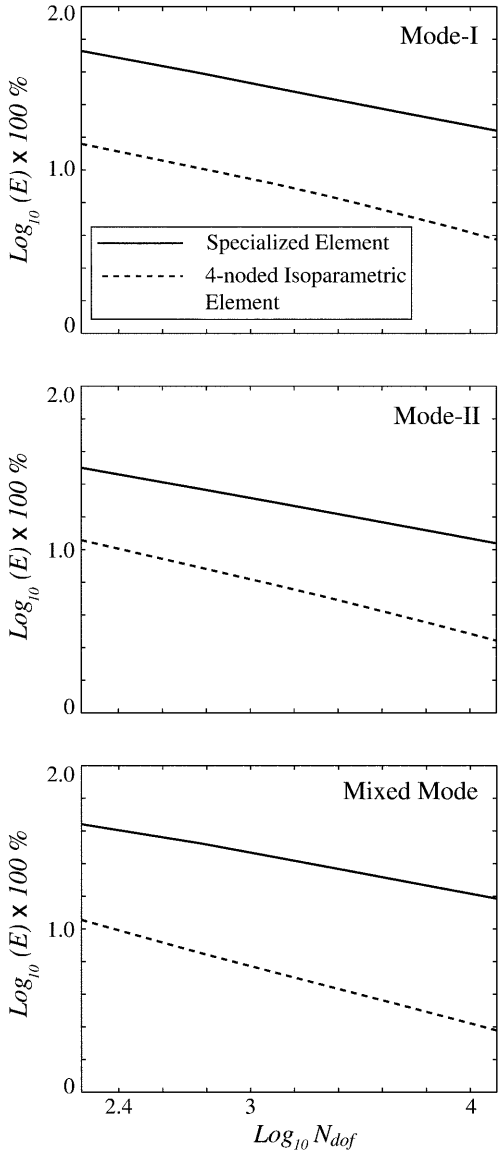

Fig. 14. The relative errors in the normalized mid-plane deformation vector $\frac{1}{a}\{U_x, U_y, U_{xy}\}$ associated with the specialized element (solid lines) and those in the mid-plane strains of the 4-noded isoparametric element (dashed lines) are plotted against the corresponding number of degrees of freedom N_{dof} in a log–log scal

However, in [21], Kuhn compared the predictions from 3-D finite element analysis of the woven unit-cell and those obtained from the semi-analytical method (see [1]) employing the very shape functions employed in the specialized element for three different in-plane boundary value problems. The predictions from the semi-analytical method compared favorably to their 3-D finite element counterparts and exhibited superior computational advantages over computationally demanding 3-D finite element method.

4 Conclusion

A specialized finite element for woven composites has been developed utilizing recently developed displacement fields for woven composites in its displacement interpolation scheme. The element formulation, which incorporates robust unit-cell geometry models for both polymer and ceramic matrix woven systems, is carried out with the aid of an asymptotic expansion displacement form that accounts for the homogenized solution and the periodic micro-displacement contribution associated with the local unit-cell elasto-statics problem. As such, the element is capable of predicting both the macroscopic homogeneous and the microscopic elastic responses of a finite geometry of woven composites subjected to a general in-plane loading. As presented, the proposed element exhibits acceptable accuracy while retaining computational efficiency. The proposed element's unique capability of capturing the micro-elastic fields provides detailed micro-stress distribution of such systems, for the first time. With the efficiency and reliability of the proposed element demonstrated through this work, the element is expected to broaden the scope of study on woven composites, and is expected to enable the development of robust analysis tools for a wide range of heterogeneous systems exhibiting complex microstructures.

References

1. **Kuhn JL, Haan SI, Charalambides PG** (1999) A semi-analytical method for the calculation of the elastic micro-fields in plain weave fabric composites subjected to in-plane loading. J. Composite Mater. 33(3): 221–266
2. **Ishikawa T, Chou T-W** (1982) Elastic behavior of woven hybrid composites. J. Composite Mater. 16: 2–19
3. **Ishikawa T, Chou T-W** (1982) Stiffness and strength behaviour of woven fabric composites. J. Mater. Sci. 17: 3211–3220
4. **Ishikawa T, Chou T-W** (1983) In-plane thermal expansion and thermal bending coefficients of fabric composites. J. Composite Mater. 17: 92–104
5. **Ishikawa T, Chou T-W** (1983) One-dimensional micromechanical analysis of woven fabric composites. AIAA J. 21(12): 1714–1721
6. **Chou T-W, Ishikawa T** (1989) Analysis and modeling of two-dimensional fabric composites. In: Chou T-W, Ko FK, (eds), Textile Structural Composites: Composite Materials Series, Vol. 3, Elsevier Science Publishers B.V., pp. 209–264
7. **Naik NK, Shembekar PS** (1992) Elastic behavior of woven fabric composites: I-lamina analysis. J. Composite Mater. 26(15): 2196–2225
8. **Naik NK, Ganesh VK** (1992) Prediction of on-axes elastic properties of plain weave fabric composites. Composites Sci & Tech. 45: 135–152
9. **Vaidyanathan KR, Kelkar AD, Sankar J** (1993) Prediction of elastic properties of ceramic matrix composites using a plain weave classical laminate theory. Ceram. Engr. Sci. Proc. 14(9–10): 1066–1076
10. **Raju IS, Wang JT** (1994) Classical laminate theory models for woven fabric composites. J. Composite Tech. & Res. 16(4): 289–303
11. **Kuo W-S, Chou T-W** (1995) Elastic response and effect of transverse cracking in woven fabric brittle matrix composites. J. Amer. Ceram. Soc. 78(3): 783–792
12. **Zhang YC, Harding J** (1990) A numerical micromechanics analysis of the mechanical properites of a plain weave composite. Comput. Struct. 36(5): 839–844
13. **Whitcomb JD** (1991) Three-dimensional stress analysis of plain weave composites. In: O'Brien TK (ed) Composite Materials: Fatigue and Fracture, Vol. 3, ASTM STP 1110, Amer-

ican Society for Testing and Materials, Philadelphia, pp. 417–438
14. **Dasgupta A, Bhandarkar SM** (1994) Effective thermomechanical behavior of plain-weave fabric-reinforced composites using homogenization theory. J. Engr. Mater. & Tech. 116: 99–105
15. **Kuhn JL, Charalambides PG** (1999) Modeling of plain weave fabric composite geometry. J. Composite Mater. 33(3): 187–220
16. **Kuhn JL, Charalambides PG** (1998) Elastic response of porous matrix plain weave fabric composites: Part II – Results. J. Composite Mater. 32(16): 1472–1507
17. **Kuhn JL, Haan SI, Charalambides PG** (2000) Stress-induced matrix microcracking in brittle matrix plain weave fabric composites under uniaxial tension. J. Composite Mater. 34(19): 1640–1664
18. **Haan SI, Charalambides PG, Kuhn JL, Patterson MCL** (2000) Supercritical matrix microcracking in brittle matrix plain weave composites under uniaxial tension. Submitted to Mech. Mater
19. **Haan SI, Charalambides PG** (2000) Concurrent evolution of multiple types of damage in CVI woven CMCs subjected to uniaxial tension. Submitted to J. Composite Mater.
20. **Kuhn JL, Charalambides PG** (1998) Elastic response of porous matrix plain weave fabric composites: Part I – modeling. J. Composite Mater. 32(16): 1426–1471
21. **Kuhn JL** (1997) Mechanical behavior of woven ceramic composites. PhD Thesis, University of Maryland Baltimore County
22. **Bensoussan A, Lions JL, Papanicolaou G** (1978) Asymptotic analysis for periodic structures
23. **Oleinik OA, Shamaev AS, Yosifian GA** (1992) Mathematical problems in elasticity and homogenization. Studies Math. Appl.
24. **Cioranescu D, Paulin JST** (1999) Homogenization of reticulated structures. Applied Math. Sci.
25. **Wahlbin LB** (1984) On the sharpness of certain estimates for H projection into finite element spaces: influence of a reentrant corner. Math. Camp. 42: 1–8
26. **Sih GC, Paris PC, Irwin H** (1965) On cracks in rectilinearly anisotropic bodies. Int. J. Fracture Mech. 1: 189–203